Molybdenum–Ruthenium–Carbon Solid-Solution Alloy Nanoparticles: Can They Be *Pseudo*-Technetium Carbide?

Shinya Okazoe,[1] Kohei Kusada,[1,2,*] Yukihiro Yoshida,[1,*] Mitsuhiko Maesato,[1,*] Tomokazu Yamamoto,[3] Takaaki Toriyama,[3] Syo Matsumura,[3,4,†] Shogo Kawaguchi,[5] Yoshiki Kubota,[6] Yusuke Nanba,[7] Susan Meñez Aspera, [7] Michihisa Koyama[7] and Hiroshi Kitagawa[1,*]

[1] Division of Chemistry, Graduate School of Science, Kyoto University, Kitashirakawa-Oiwakecho, Sakyo-ku, Kyoto 606-8502, Japan. [2] The Hakubi Center for Advanced Research, Kyoto University, Kitashirakawa-Oiwakecho, Sakyo-ku, Kyoto 606-8502, Japan. [3] The Ultramicroscopy Research Center, Kyushu University, Motooka 744, Nishi-ku, Fukuoka 819-0395, Japan. [4] Department of Applied Quantum Physics and Nuclear Engineering, Kyushu University, 744 Motooka, Nishi-ku, Fukuoka 819-0395, Japan. [5] Japan Synchrotron Radiation Research Institute (JASRI), SPring-8, 1-1-1 Kouto, Sayo-cho, Sayo-gun, Hyogo 679-5198, Japan. [6] Department of Physics, Graduate School of Science, Osaka Metropolitan University, 1-1 Gakuen-cho, Naka-ku, Sakai, Osaka 599-8531, Japan. [7]Research Initiative for Supra-Materials, Shinshu University, 4-17-1 Wakasato, Nagano 380-8553, Japan.

ABSTRACT: Technetium (Tc), atomic number 43, is an element that humans cannot freely use even in the 21st century because Tc is radioactive and has no stable isotope. In this report, we present molybdenum–ruthenium–carbon solid-solution alloy ($Mo_xRu_{1-x}C_y$) nanoparticles (NPs) that are expected to have an electronic structure similar to that of technetium carbide (TcC_y). $Mo_xRu_{1-x}C_y$ NPs were synthesized by annealing under a helium/hydrogen atmosphere following a thermal decomposition of metal precursors. The obtained NPs had a solid-solution structure in the whole composition range. $Mo_xRu_{1-x}C_y$ with a cubic structure (down to 30 at% Mo in the metal ratio) showed a superconducting state, and the transition temperature (T_c) increased with increasing Mo composition. The continuous change in T_c across that of TcC_y indicates the continuous control of electronic structure by solid-solution alloying, leading to *pseudo*-TcC_y. Density functional theory (DFT) calculations indicated that the synthesized $Mo_{0.53}Ru_{0.47}C_{0.41}$ has a similar electronic structure to $TcC_{0.41}$.

INTRODUCTION

Technetium (Tc), atomic number 43, is the first artificially made element.[1] As Tc can only be obtained from a nuclear reactor or fission product of uranium,[1] the amount of production of Tc is limited compared with elements present in nature. In addition to this, Tc is radioactive and has no stable isotope. Therefore, the use of Tc is limited to diagnostic nuclear medicine applications,[2] and properties of Tc and its compounds are still veiled[3] despite the fact that it was discovered about 80 years ago.

Up to now, a wide variety of alloy nanoparticles (NPs) have been synthesized and are currently being used in various applications such as catalysts.[4-9] Recently, solid-solution alloy NPs whose constituent atoms are distributed homogeneously have attracted increasing interest including bulk-immiscible systems because those with a desired composition can control the electronic structure and provide new and more advanced properties that surpass the pristine NPs.[10-13] Our group has already explored several solid-solution alloy NPs. For example, the formation of Pd_xRu_{1-x} solid-solution alloy NPs,[10] in which Pd and Ru both neighboring on Rh are immiscible in bulk, have a catalytic activity of nitrogen oxides reduction greater than that of Rh NPs.[11] In addition, Au_xIr_{1-x} solid-solution alloy NPs, in which Au and Ir both neighboring on Pt are immiscible in bulk, showed a high oxygen reduction reaction activity comparable to that of Pt NPs.[12] As another example, Ag_xRh_{1-x} solid-solution alloy NPs showing hydrogen adsorption properties similar to Pd neighboring on Ag and Rh have already been reported.[13] These significant achievements strongly indicate that the electronic structure, especially the density of states (DOS) near the Fermi level (E_F), $N(E_F)$, of the NPs would resemble closely that of the element interposed by the two constituent elementals on the periodic table of the elements by solid-solution alloying.[11] However, these studies offer substitutes for elements present in nature whose properties have been investigated well.

Radioactive and rare in nature, Tc undergoes a superconducting transition at a critical temperature (T_c) of 7.7 K.[14] Given that Mo and Ru both neighboring on Tc show a superconducting transition only below 1 K,[15] Mo–Ru solid-solution alloy is a promising platform for investigating the modulation of electronic structure by solid-solution alloying through monitoring T_c. In this regard, theoretical calculations predicted that the Mo–Ru solid-solution alloy with a 1:1 molar ratio can reproduce the electronic structure of Tc.[16] We note that the difficulty in elucidating the chemical and physical characteristics of radioactive Tc can be partially overcome by the "artificial" Tc formed by the solid-solution alloying of Mo and Ru.

Keeping in mind the presented issues, we pursued Mo–Ru solid-solution alloy NPs that can be regarded as *pseudo*-Tc. However, Mo–Ru solid-solution alloy NPs in which carbon

atoms are included in the lattice, namely Mo–Ru–C solid-solution alloy ($Mo_xRu_{1-x}C_y$) NPs, were obtained.

In this study, we synthesized $Mo_xRu_{1-x}C_y$ over the whole composition range and experimentally verified whether $Mo_xRu_{1-x}C_y$ can be regarded as technetium carbide (TcC_y). The distinct T_c value of cubic TcC_y is 3.8 K,[17] lying between those of cubic molybdenum carbide (MoC_y: 12 K)[18] and cubic ruthenium carbide (RuC_y: no observation). $Mo_xRu_{1-x}C_y$ having comparable T_c with that of TcC_y would have a similar electronic structure to that of TcC_y. We demonstrate the homogeneous distribution of Mo and Ru atoms in the NPs and the continuous change in superconducting behavior as manifested in T_c for the first time. DFT calculations indicated that the synthesized $Mo_{0.53}Ru_{0.47}C_{0.41}$ has a similar electronic structure to $TcC_{0.41}$.

RESULTS AND DISCUSSION

Referring to our previous report,[19] $Mo_xRu_{1-x}C_y$ (x: 0~1.0) were synthesized by thermal decomposition of molybdenum hexacarbonyl ($Mo(CO)_6$) and/or triruthenium dodecacarbonyl ($Ru_3(CO)_{12}$) in oleylamine at 330 °C for 2 h followed by annealing up to 800 °C under helium/hydrogen (96/4 vol%) atmosphere. The synthetic details are described in SI. The nominal amounts of precursor metal complexes and the metal composition of $Mo_xRu_{1-x}C_y$ determined by X-ray fluorescence (XRF) spectrometry are shown in Table S1.

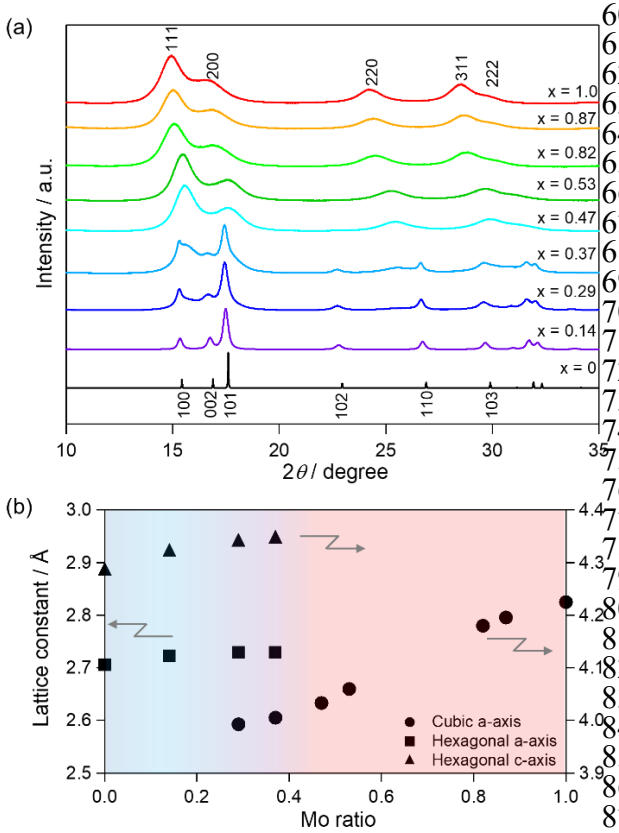

Figure 1. (a) Comparison of PXRD patterns between 10 to 35° of $Mo_xRu_{1-x}C_y$. X-ray wavelength was 0.62921(4) Å. The numbers near the diffraction pattern indicate the Miller indices of cubic (for x = 1.0) and hexagonal (for x = 0) phases, respectively. (b) Lattice constants of cubic (circles) and hexagonal (squares and triangles) structures estimated from Le Bail refinement.

To unveil the crystal structure of $Mo_xRu_{1-x}C_y$, synchrotron powder X-ray diffraction (PXRD) analysis was performed. Figure 1a shows a comparison of PXRD patterns between 2θ = 10 and 35° of $Mo_xRu_{1-x}C_y$. The results of Le Bail refinement are shown in Figures S1–S3. The PXRD patterns of $Mo_xRu_{1-x}C_y$ in Mo-rich compositions were fitted with a cubic structure (space group: $Fm\bar{3}m$), whereas those of Ru-rich compositions were fitted with a hexagonal structure (space group: $P6_3/mmc$). The PXRD patterns of the intermediate states ($Mo_{0.37}Ru_{0.63}C_y$ and $Mo_{0.29}Ru_{0.71}C_y$) were fitted using these two structures. The PXRD patterns of the cubic phase are closely similar to that of the cubic MoC_y among various molybdenum carbides,[18, 20-21] in which carbon atoms occupy the octahedral site of face-centered cubic (fcc) structured metal lattice (Figure S4). Therefore, $Mo_xRu_{1-x}C_y$ with a cubic structure is considered to be a cubic metal carbide. Although the crystallite size of the cubic component is almost constant at around 3 nm in all the samples (Figure S5), that of the hexagonal component decreases with increasing Mo ratio. As shown in Figure 1b, the lattice constants of the cubic and hexagonal structures increase linearly with increasing Mo ratio. The linear correlation, which follows an approximate empirical rule known as Vegard's law,[22] strongly supports the formation of the atomic-level Mo–Ru solid-solution alloy over the whole composition range.

It is well known that the lattice constant of transition metal carbides reflects the amount of carbon in their lattice.[23,24] In this paper, the carbon amount in the lattice of $Mo_xRu_{1-x}C_y$ was estimated from lattice constants. We first consider the case of x = 1.0, namely MoC_y (lattice constant from PXRD measurement: 4.2249 Å).[19] Assuming that the amount of carbon is linearly proportional to the lattice constant at a specific metal composition, the y value in MoC_y was estimated to be 0.59 from the lattice constants of ideal fcc $Mo_{1.0}$ (3.920 Å) with closely packed Mo atoms (atomic radius: 1.386 Å)[25] and that of $MoC_{0.681}$ prepared previously (4.26647 Å).[18] In the case of x < 1, namely solid-solution alloys, the lattice constant decreases with decreasing x because of the smaller atomic radius of Ru (1.336 Å)[25] than that of Mo. The carbon amounts of $Mo_xRu_{1-x}C_y$ were estimated in the same way as the case of x = 1.0 (e.g., 0.41 for x = 0.53; Figure S6b), where the lattice constants of ideal Mo_xRu_{1-x} and $Mo_xRu_{1-x}C_{0.681}$ were calculated taking into account the metal substitution (Figure S6a; see SI for the details). Hereafter, we denote samples in cubic phase with the carbon amount, for example, $Mo_{0.53}Ru_{0.47}C_y$ is described as $Mo_{0.53}Ru_{0.47}C_{0.41}$. The change in carbon ratio toward metal composition can be explained using thermodynamic parameters. The formation enthalpy of cubic MoC is negative, whereas that of cubic RuC is positive,[26] indicating that the formation of $Mo_xRu_{1-x}C_y$ may become enthalpy-unfavored in Ru-rich composition. Therefore, the amount of carbon is considered to decrease with decreasing Mo ratio. We note that the measured lattice constant in a hexagonal close-packed (hcp) phase is close to that of ideal hcp Mo_xRu_{1-x} (Figure S7), indicating that hexagonal Mo_xRu_{1-x} may contain a negligible amount of carbon atoms compared with fcc Mo_xRu_{1-x}. The formation of cubic $Mo_xRu_{1-x}C_y$ was also supported by X-ray absorption near-edge structure (XANES)

spectra. Figures S8–S14 show the XANES spectra at Mo and Ru *K*-edges of $Mo_xRu_{1-x}C_y$. It is known that the energy of the absorption edge reflects the valence of the element.[27] Here, the energy at the midpoint of the edge jump is defined as E_0 and the energy shift of E_0 from the reference metals (Mo and Ru) was compared (Figure S15). The Mo *K*-edge XANES spectra of $Mo_xRu_{1-x}C_y$ in the cubic phase (x = 1.0, 0.87, and 0.53) are similar to the reference Mo_2C spectrum that resembles that of cubic MoC.[28] Furthermore, the energy difference of the cubic phase (x = 1.0, 0.87, and 0.53) in Mo *K*-edge was comparable to that of cubic MoC_y (c.a. 1~2 eV),[29] indicating the inclusion of carbon atoms in the cubic phase. On the other hand, the energy difference of the hexagonal phase (x = 0.14 and 0) in Mo and Ru *K*-edge were almost zero, indicating that $Mo_xRu_{1-x}C_y$ with the hexagonal phase is a metallic state.

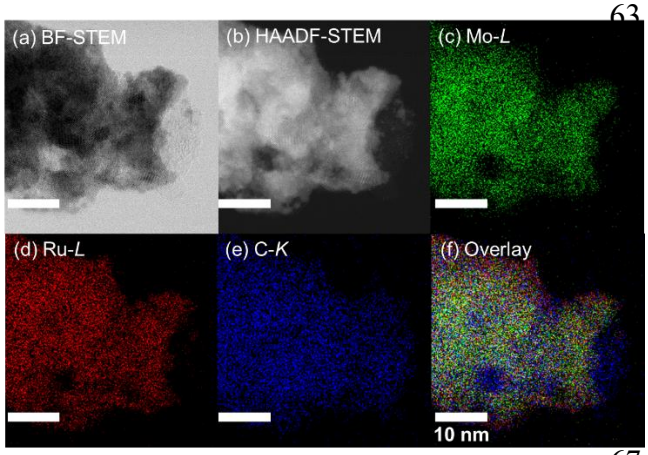

Figure 2. (a) Bright-field (BF) STEM image; (b) high-angle annular dark-field (HAADF) STEM image; (c) Mo-*L* (d) Ru-*L*, and (e) C-*K* EDX maps; and (f) overlay images of $Mo_{0.53}Ru_{0.47}C_{0.41}$. Scale bars are 10 nm.

To confirm the morphologies of $Mo_xRu_{1-x}C_y$, transmission electron microscopy (TEM) observation was performed (Figures S16–S22). Although the size of aggregates substantially exceeds 100 nm, single nanosized particles were observed at the edges of the aggregates in Mo-rich composition. On the other hand, each particle composing the aggregates was around 10 nm in size in Ru-rich composition. In $Ru_{1.0}C_y$, over 100 nm aggregates were observed. As seen in Figure 2, scanning TEM (STEM) energy dispersive X-ray spectroscopy (EDX) maps for nearly 1:1 solid-solution alloy NPs, $Mo_{0.53}Ru_{0.47}C_{0.41}$, clearly show that the Mo and Ru atoms are homogeneously distributed in NPs. The line analyses also support the solid-solution structure (Figure S23). The C-*K* EDX map reveals that carbon species are covering NPs besides the carbon in the lattice, which was also confirmed by the electron energy loss spectroscopy (EELS) map (Figure S24). These carbon species were assigned as graphite-like carbon by Raman spectroscopy because the G and D bands[30] that are characteristic vibration modes of graphite were observed at around 1600 and 1350 cm^{-1}, respectively, as previously reported (Figure S25).[19] Similar structural features, i.e., NPs with homogeneous distributions of Mo and Ru covered by graphite-like carbon were also observed with other metal compositions (Figures S23, S25–S29). The synthesized NPs in the cubic phase have similar morphology and crystallite size, which exclude the morphology and size effects on chemical and physical properties.

To investigate physical properties, we measured the electrical resistivity and magnetism at low temperatures. Figure 3a shows the temperature dependence of resistivity (ρ) of a compaction pellet of $Mo_{0.53}Ru_{0.47}C_{0.41}$ under H = 0 kOe. A rapid drop in resistivity started at 4.1 K with a transition width of ca. 1.7 K. Figure 3b shows the temperature dependence of magnetic susceptibility ($\chi = M/H$, where M and H are the magnetization and applied magnetic field, respectively) of $Mo_{0.53}Ru_{0.47}C_{0.41}$ in zero-field cooling (ZFC) and field cooling (FC) under H = 10 Oe. A sharp diamagnetic drop was observed at 2.5 K because of the Meissner effect. The significant superconducting volume fraction value (66%) strongly demonstrates the existence of the bulk superconducting state.

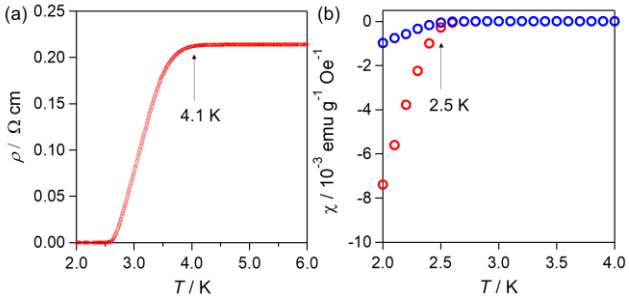

Figure 3. (a) Temperature dependence of ρ of $Mo_{0.53}Ru_{0.47}C_{0.41}$ at 0 Oe. (b) Temperature dependence of χ of $Mo_{0.53}Ru_{0.47}C_{0.41}$ at 10 Oe (red circles: ZFC; blue circles: FC).

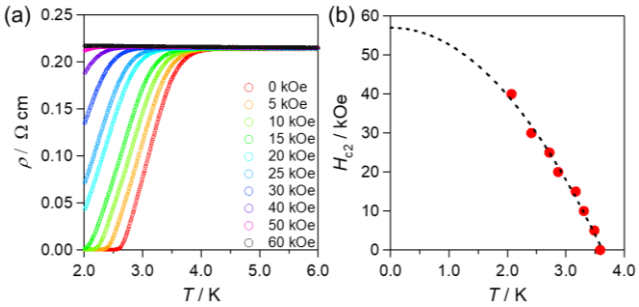

Figure 4. (a) Temperature dependence of ρ of $Mo_{0.53}Ru_{0.47}C_{0.41}$ under different magnetic fields. (b) Magnetic field dependence of H_{c2} was estimated from the resistivity measurements. The broken curve is fitted to $H_{c2}(T) = H_{c2}(0)(1-(T/T_c)^2)$.

Temperature-dependent resistivity under different magnetic fields was measured to evaluate the stability of superconductivity (Figure 4a). The data of Figure 3a are replotted to show the variation of resistivity behavior by applying a magnetic field. The sharp drop remains even under the highest magnetic field of 60 kOe. Provided that a point where the ρ reaches 90% of that at 6.0 K which is defined as the upper critical field ($H_{c2}(T)$) at a certain temperature, $H_{c2}(0)$ was estimated to be 57 kOe by extrapolation using $H_{c2}(T) = H_{c2}(0)(1-(T/T_c)^2)$ for a weakly coupled superconductor (Figure 4b).[20,31] It is noteworthy that the estimated $H_{c2}(0)$ value lies within the Pauli paramagnetic limit field (H_{Pauli} = 75 kOe) as given by the weak coupling Bardeen–

Cooper–Schrieffer (BCS) approximation, H_{Pauli} [T] = 1.84T_c [K].[32] The Ginzburg–Landau coherence length ξ_{GL} at T = 0 K, correlating with $H_{c2}(0)$ as $\xi_{GL} = (\phi_0/2\pi H_{c2}(0))^{1/2}$ (ϕ_0: flux quantum),[33] was calculated to be 7.6 nm. Given that the ξ_{GL} value is greater than the separation of NPs (the separation distance was estimated to be 0.3 nm; Figure S30), it is evident that the carbon species embedded with superconducting NPs is also in a superconducting state by the proximity effect as observed on analogous system.[34]

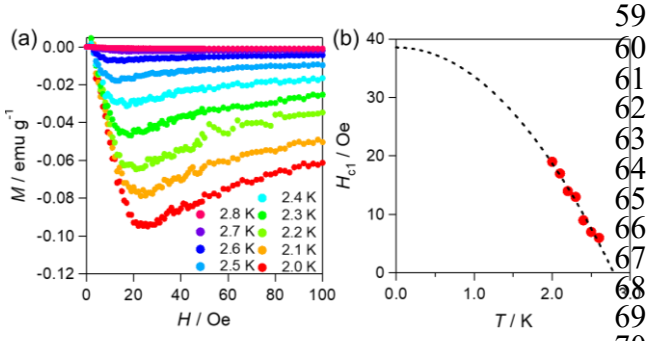

Figure 5. (a) Isothermal magnetization curves of $Mo_{0.53}Ru_{0.47}C_{0.41}$ under different temperatures with 0.1 K interval. (b) Temperature dependence of H_{c1} by magnetization measurements. A broken curve is fitted to $H_{c1}(T) = H_{c1}(0)(1-(T/T_c)^2)$.

The isothermal magnetization curve of $Mo_{0.53}Ru_{0.47}C_{0.41}$ was measured at different temperatures to estimate the lower critical field (H_{c1}). The magnetization curves are characteristic of type-II superconductors; namely, the gradual diminishment of diamagnetism above the initial flux penetration field (Figure 5a). Provided that the separation point from a straight line in the magnetization curve at each temperature is defined as H_{c1}, $H_{c1}(0)$ was estimated to be 38 Oe by extrapolation using a conventional equation for a weakly coupled superconductor (Figure 5b), $H_{c1}(T) = H_{c1}(0)(1-(T/T_c)^2)$.[20,31] Using the estimated $H_{c1}(0)$ value, the London penetration depth ($\lambda(0)$) was estimated to be 4.3×10^2 nm according to the equation, $H_{c1}(T) = (\phi_0/4\pi\lambda^2)\ln(\lambda/\xi_{GL})$.[35] Thus, the Ginzburg–Landau parameter $\kappa(0)$, which is defined as $\kappa(0) = \lambda(0)/\xi_{GL}(0)$, of 57 again confirmed the type-II superconductivity in $Mo_{0.53}Ru_{0.47}C_{0.41}$.

The lower T_c compared with that of bulk cubic MoC_y (T_c = 12 K[18]) may be associated with the size-induced discretization of the energy levels.[36] Similar size-dependent behavior was observed in MoC_y.[37] The superconducting parameter that was most affected by nano-sizing is $\lambda(0)$ (4.3×10^2 nm *vs.* 1.3×10^2 nm in bulk MoC_y[18]). The increased $\lambda(0)$ possibly arises from the depression of the surface shielding current by reducing the particle size.[38]

Figure 6 displays the relationship between the Mo ratio and onset T_c determined by magnetic susceptibility and resistivity measurements in the present $Mo_xRu_{1-x}C_y$ (Figure S31). The T_c value is the highest at x = 1.0 (6.4 K)[19] and gradually decreases with decreasing Mo ratio. $Mo_xRu_{1-x}C_y$ with x < 0.3 showed no trace of superconductivity down to the lowest measured temperature (2 K). These results indicate that only the cubic phase shows superconductivity above 2 K, and the T_c value varies continuously across that of TcC_y depending on metal composition, possibly as a consequence of the homogeneous distribution of Mo and Ru at the atomic level.

We performed DFT calculations to evaluate the similarity of electronic structures between $Mo_xRu_{1-x}C_y$ with nearly the equivalent metal composition and TcC_y with the same carbon amount. $Mo_{17}Ru_{15}C_{13}$ ($Mo_{0.531}Ru_{0.469}C_{0.406}$) and $Tc_{32}C_{13}$ ($TcC_{0.406}$) were constructed as model structures (Figure S32). The DFT calculations elucidated that the DOS profile of $Mo_{17}Ru_{15}C_{13}$ was very similar to that of $Tc_{32}C_{13}$ (Figure 7).

According to the BCS theory, T_c is correlated to $N(E_F)$ by the following equation, $k_BT_c = 1.14\hbar\omega\exp[-1/VN(E_F)]$, where $\hbar$, ω, and V are reduced Planck constant, frequency of lattice vibration, and electron–phonon interaction, respectively.[35,39] Assuming that ω and V are approximately invariant with the Mo ratio, the increased T_c for the Mo-rich phase (Figure S33) may be associated with the increased $N(E_F)$. Three major factors depending on the composition can affect $N(E_F)$; namely, (i) downshift of E_F with increasing Mo ratio, (ii) lattice expansion, and (iii) modified electronic structure depending on the amount of carbon in the lattice. It is apparent that the third factor has little effect on T_c because the partial DOS of carbon near E_F is not pronounced (Figure S34). On the other hand, the downshift of the Fermi level by substituting Ru by Mo in cubic C increases $N(E_F)$ within the rigid band approximation (Figure 7), which could modify the electronic structure in the favorable direction of increased T_c as observed. The metal substitution of Ru to Mo also results in the increased $N(E_F)$ owing to the lattice expansion. Accordingly, we successfully demonstrated the continuous control of $N(E_F)$, which is one of the typical physical parameters representing electronic structure, of ternary solid-solution alloy NPs by changing the metal composition.

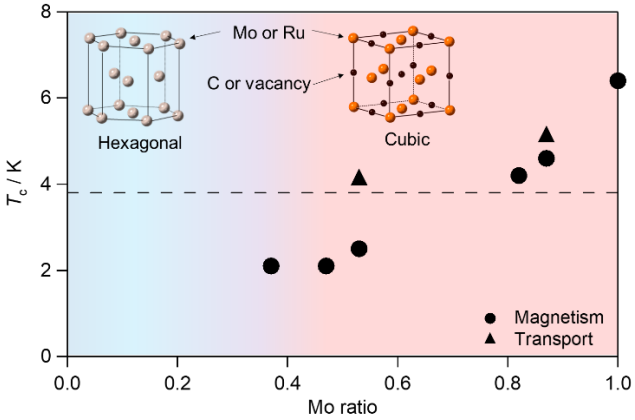

Figure 6. Relationship between Mo ratio and T_c of $Mo_xRu_{1-x}C_y$. Circles and triangles indicate T_c estimated from magnetic and resistivity measurements, respectively. The T_c values of $MoC_{0.59}$ and $Mo_{0.87}Ru_{0.13}C_{0.60}$ are from ref. 19. The broken line at 3.8 K indicates T_c of TcC_y.[17] The pale red and blue areas show the composition that adopts cubic and hexagonal structures, respectively.

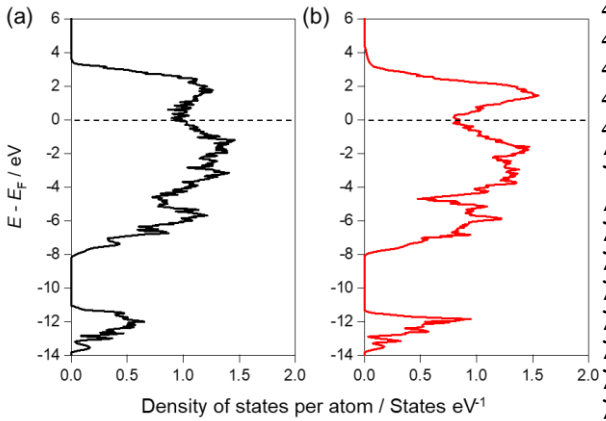

Figure 7. Calculated total DOS distributions of cubic (a) $Mo_{17}Ru_{15}C_{13}$ and (b) $Tc_{32}C_{13}$. M_{PCC} of $Mo_{17}Ru_{15}C_{13}$ toward $Tc_{32}C_{13}$, which is the index of the similarity,[40] was estimated to be 0.96 (see SI for the details).

CONCLUSION

In this report, $Mo_xRu_{1-x}C_y$ solid-solution alloy NPs were synthesized by annealing under a He/H_2 atmosphere following a thermal decomposition. The obtained NPs have a solid-solution structure over the entire composition range. $Mo_xRu_{1-x}C_y$ solid-solution alloy NPs (up to 30 at% Mo in the metal ratio) showed type-II superconductivity. Reflecting the homogeneous distribution of Mo and Ru at the atomic level, systematic change in T_c can best be thought of as a continuous change in electronic structure across TcC_y by alloying. DFT calculations indicated that $Mo_{0.53}Ru_{0.47}C_{0.41}$ has a similar electronic structure to $TcC_{0.41}$. Namely, it is plausible that the answer to the title of this article is partly yes because the $N(E_F)$, which plays a vital role in many physical and chemical phenomena of cubic $Mo_xRu_{1-x}C_y$, such as transport, magnetism, and catalysis, was found to be similar to that of isomorphous TcC_y.

EXPERIMENTAL SECTION

Synthesis of $Mo_xRu_{1-x}C_y$. Oleylamine was evacuated under 2 kPa at 100 °C for 1 h to remove residual water. After purging with nitrogen gas, $Mo(CO)_6$ and/or $Ru_3(CO)_{12}$ were added to oleylamine, and the solution was heated at 330 °C for 2 h. The product was separated by centrifugation with hexane and acetone. Subsequently, the product was annealed up to 800 °C under helium/hydrogen atmosphere (96/4 vol%) with a heating rate of 5 °C min^{-1} using BELCAT (Microtrac BEL). After reaching 800 °C, the sample was cooled down to room temperature under helium/hydrogen atmosphere.

Characterization of $Mo_xRu_{1-x}C_y$. The crystal structures of the NPs were determined by synchrotron PXRD measurements (λ = 0.62921(4) Å, scan step: 0.006°) at SPring-8 beamline BL02B2. Le Bail refinement of the PXRD pattern was performed using TOPAS3 (Bruker AXS). XANES spectra were obtained in transmission mode using a Si(311) double crystal monochromator at SPring-8 beamline BL14B2. The morphologies of NPs were observed using an HT7700 (Hitachi) TEM operated at 100 kV. Bright-field (BF) and high-angle annular dark-field (HAADF)-STEM observation, STEM-EDX mapping and line analysis, and EELS mapping were performed using an aberration-corrected electron microscope JEM-ARM 200F (JEOL) operated at 120 kV. Raman scattering measurements were performed with an NRS-5100 Raman spectrometer (JASCO) with a 532 nm excitation laser.

Evaluation of superconductivity. Magnetic susceptibility measurements were performed by an MPMS-XL superconducting quantum interference device magnetometer (Quantum Design). Plastic wrap and straw were used as sample holders. After the sample was cooled to 2 K, a magnetic field of 10 Oe was applied. The temperature was swept between 2 K and 8 K in ZFC and FC measurements. For the magnetization process measurements, the magnetic field was applied after the sample was cooled to the measuring temperature. The present data are shown after subtracting the contribution of straw and wrap used as sample holders. The DC resistivity in the temperature range from room temperature to 2.0 K was measured with a four-probe method using a physical properties measurement system (PPMS, Quantum Design) to measure T_c and H_{c2}. A compressed pellet with 2.5 mm in diameter was made by pressing the powder sample at 1 GPa for 10 min. Gold wires 15 μm in diameter were attached to the compressed pellet with carbon paste as electrodes.

ASSOCIATED CONTENT

Experimental details, XRF results, Le Bail fitting of PXRD patterns, thermogravimetric analysis, XANES spectra, TEM images, EDX line analysis, EELS maps, Raman spectroscopy, superconductive measurements of $Mo_xRu_{1-x}C_y$, DFT calculation are shown in the Supporting Information. These materials are available free of charge via the Internet at http://pubs.acs.org.

AUTHOR INFORMATION

Corresponding Author

Kohei Kusada – Division of Chemistry, Graduate School of Science, Kyoto University, Kitashirakawa-Oiwakecho, Sakyo-ku, Kyoto 606-8502, Japan.; The Hakubi Center for Advanced Research, Kyoto University, Kitashirakawa-Oiwakecho, Sakyo-ku, Kyoto 606-8502, Japan.; E-mail: kusada@kuchem.kyoto-u.ac.jp
Yukihiro Yoshida – Division of Chemistry, Graduate School of Science, Kyoto University, Kitashirakawa-Oiwakecho, Sakyo-ku, Kyoto 606-8502, Japan.; E-mail: yoshiday@ssc.kuchem.kyoto-u.ac.jp
Mitsuhiko Maesato – Division of Chemistry, Graduate School of Science, Kyoto University, Kitashirakawa-Oiwakecho, Sakyo-ku, Kyoto 606-8502, Japan.; E-mail: maesato@kuchem.kyoto-u.ac.jp
Hiroshi Kitagawa – Division of Chemistry, Graduate School of Science, Kyoto University, Kitashirakawa-Oiwakecho, Sa-kyo-ku, Kyoto 606-8502, Japan.; E-mail: kitagawa@kuchem.kyoto-u.ac.jp

Authors

Shinya Okazoe – Division of Chemistry, Graduate School of Science, Kyoto University, Kitashirakawa-Oiwakecho, Sakyo-ku, Kyoto 606-8502, Japan.
Tomokazu Yamamoto – The Ultramicroscopy Research Center, Kyushu University, Motooka 744, Nishi-ku, Fukuoka 819-0395, Japan.

Takaaki Toriyama – The Ultramicroscopy Research Center, Kyushu University, Motooka 744, Nishi-ku, Fukuoka 819-0395, Japan.
Syo Matsumura – The Ultramicroscopy Research Center, Kyushu University, Motooka 744, Nishi-ku, Fukuoka 819-0395, Japan.; Department of Applied Quantum Physics and Nuclear Engineering, Kyushu University, 744 Motooka, Nishi-ku, Fukuoka 819-0395, Japan.
Shogo Kawaguchi – Japan Synchrotron Radiation Research Institute (JASRI), SPring-8, 1-1-1 Kouto, Sayo-cho, Sayo-gun, Hyogo 679-5198, Japan.
Yoshiki Kubota – Department of Physics, Graduate School of Science, Osaka Metropolitan University, 1-1 Gakuen-cho, Naka-ku, Sakai, Osaka 599-8531, Japan.
Yusuke Nanba – Research Initiative for Supra-Materials, Shinshu University, 4-17-1 Wakasato, Nagano 380-8553, Japan.
Susan Meñez Aspera – Research Initiative for Supra-Materials, Shinshu University, 4-17-1 Wakasato, Nagano 380-8553, Japan.
Michihisa Koyama – Research Initiative for Supra-Materials, Shinshu University, 4-17-1 Wakasato, Nagano 380-8553, Japan.

Present Addresses

†**Syo Matsumura –** National Institute of Technology, Kurume College, 1-1-1 Komorino, Kurume, Fukuoka, 830-8555, Japan.

Notes

There are no conflicts to declare.

ACKNOWLEDGMENT

This work was supported by ACCEL from the Japan Science and Technology Agency (JST), Grant No. JPMJAC1501, Grant-in-Aid for Specially Promoted Research, No. 20H05623 and Grant-in-Aid for Scientific Research (B), No. 21H01762, and JSPS KAKENHI Grant No. 19J15102, Japan. Synchrotron PXRD measurements were conducted at BL02B2 at SPring-8 with the approval of the Japan Synchrotron Radiation Research Institute (JASRI, Proposal No. 2020A1130). XAS measurements were conducted at BL14B2 at SPring-8 with the approval of JASRI (Proposal No. 2020A1696). STEM observations were performed as part of a program conducted by the Advanced Characterization Nanotechnology Platform sponsored by The Ministry of Education, Culture, Sports, Science and Technology (MEXT), Japan.

ABBREVIATIONS

BF, Bright field; DOS, Density of states; EDX, Energy dispersive X-ray spectroscopy; EELS, Electron energy loss spectroscopy; FC, Field cooling; Fcc, Face-centered cubic; HAADF-STEM, High-angle annular dark-field scanning transmission electron microscopy; Hcp, Hexagonal close packed; MoC_y, Molybdenum carbide; NPs, Nanoparticles; PXRD, Powder X-ray diffraction; RuC_y, Ruthenium carbide; Tc, Technetium; TcC_y, Technetium carbide; TEM, Transmission electron microscopy; XANES, X-ray absorption near-edge structure; XRF, X-ray fluorescence spectrometry; ZFC, Zero-field cooling

REFERENCES

(1) Perrier, C.; Segrè, E. Technetium: The Element of Atomic Number 43. *Nature* **1947**, *159*, 24.

(2) Papagiannopoulou, D. Technetium-99m Radiochemistry for Pharmaceutical Applications. *J. Label. Compd. Radiopharm.* **2017**, *60*, 502–520.

(3) Poineau, F.; Mausolf, E.; Jarvinen, G. D.; Sattelberger, A. P.; Czerwinski, K. R. Technetium Chemistry in the Fuel Cycle: Combining Basic and Applied Studies. *Inorg. Chem.* **2013**, *52*, 3573-3572.

(4) Ferrando, R.; Jellinek, J.; Johnston, R. L. Nanoalloys: From Theory to Applications of Alloy Clusters and Nanoparticles. *Chem. Rev.* **2008**, *108*, 845–910.

(5) Singh, A. K.; Xu, Q. Synergistic Catalysis over Bimetallic Alloy Nanoparticles. *ChemCatChem* **2013**, *5*, 652–676.

(6) Wu, L.; Mendoza-Garcia, A.; Li, Q.; Sun, S. Organic Phase Syntheses of Magnetic Nanoparticles and Their Applications. *Chem. Rev.* **2016**, *116*, 10473–10512.

(7) Kusada, K.; Wu, D.; Kitagawa, H. New Aspects of Platinum Group Metal-Based Solid-Solution Alloy Nanoparticles: Binary to High-Entropy Alloys. *Chem. Eur. J.* **2020**, *26*, 5105–5130.

(8) Xian, J.; Li, S.; Su, H.; Liao, P.; Wang, S.; Xiang, R.; Zhang, Y.; Liu, Q.; Li, G. Electrosynthesis of α-Amino Acids from NO and other NOx species over CoFe alloy-decorated Self-standing Carbon Fiber Membranes. *Angew. Chem. Int. Ed.* **2023,** *62*, e202306726.

(9) Liu, Q.; Xian, J.; Li, Y.; Zhang, Q.; Kitagawa, H.; Li, G. Self-Assembly Ultrathin Fe-Terephthalic Acid as Synergistic Catalytic Platforms for Selective Hydrogenation. *CCS Chem.* **2022,** *4*, 3275–3284.

(10) Kusada, K.; Kobayashi, H.; Ikeda, R.; Kubota, Y.; Takata, M.; Toh, S.; Yamamoto, T.; Matsumura, S.; Sumi, N.; Sato, K.; Nagaoka, K.; Kitagawa, H. Solid Solution Alloy Nanoparticles of Immiscible Pd and Ru Elements Neighboring on Rh: Changeover of the Thermodynamic Behavior for Hydrogen Storage and Enhanced CO-Oxidizing Ability. *J. Am. Chem. Soc.* **2014**, *136*, 1864–1871.

(11) Sato, K.; Tomonaga, H.; Yamamoto, T.; Matsumura, S.; Zulkifli, N. D.; Ishimoto, T.; Koyama, M.; Kusada, K.; Kobayashi, H.; Kitagawa, H.; Nagaoka, K. A Synthetic Pseudo-Rh: NOx Reduction Activity and Electronic Structure of Pd-Ru Solid-solution Alloy Nanoparticles. *Sci. Rep.* **2016**, *6*, 28265.

(12) Kusada, K.; Wu, D.; Yamamoto, T.; Toriyama, T.; Matsumura, S.; Xie, W.; Koyama, M.; Kawaguchi, S.; Kubota, Y.; Kitagawa, H. Emergence of High ORR Activity through Controlling Local Density-of-States by Alloying Immiscible Au and Ir. *Chem. Sci.* **2019**, *10*, 652–656.

(13) K. Kusada; Yamauch, M.; Kobayashi, H.; Kitagawa, H.; Kubota, Y. Hydrogen-Storage Properties of Solid-Solution Alloys of Immiscible Neighboring Elements with Pd. *J. Am. Chem. Soc.* **2010**, *132*, 15896–15898.

(14) Sekula, S. T.; Kernohan, R. H.; Love, G. R. Superconducting Properties of Technetium. *Phys. Rev.* **1967**, *155*, 364–369.

(15) Hamlin, J. J. Superconductivity in The Metallic Elements at High Pressures. *Physica C* **2015**, *514*, 59–76.

(16) Xie, W.; Koyama, M. Theoretical Design of a Technetium-like Alloy and its Catalytic Properties. *Chem. Sci.* **2019**, *10*, 5461–5469.

(17) Giorgi, A. L.; Szklarz, E. G. Superconductivity of Technetium and Technetium carbide. *J. Less Common Met.* **1966**, *11*, 455–456.

(18) Sathish, C. I.; Guo, Y.; Wang, X.; Tsujimoto, Y.; Li, J.; Zhang, S.; Matsushita, Y.; Shi, Y.; Tian, H.; Yang, H.; Li, J.; Yamaura, K. Superconducting and Structural Properties of δ-$MoC_{0.681}$ Cubic Molybdenum Carbide Phase. *J. Solid State Chem.* **2012**, *196*, 579–585.

(19) Okazoe, S.; Kusada, K.; Yoshida, Y.; Maesato, M.; Yamamoto, T.; Toriyama, T.; Matsumura, S.; Kawaguchi, S.; Kubota, Y.; Kitagawa, H. First Observation of Superconductivity in Molybdenum–Ruthenium–Carbon Alloy Nanoparticles. *Chem. Lett.* **2021**, *50*, 596–598.

(20) Yamaura, K.; Huang, Q.; Akaishi, M.; Takayama-Muromachi, E. Superconductivity in the Hexagonal-Layered Molybdenum Carbide η−Mo_3C_2. *Phys. Rev. B* **2006**, *74*, 184510.

(21) Parthé, E.; Sadogopan, V. The Structure of Dimolybdenum Carbide by Nuetron Diffraction Technique. *Acta Cryst.* **1963**, *16*, 202–205.

(22) Denton, A. R.; Ashcroft, N. W. Vegard's Law. *Phys. Rev. A* **1991**, *43*, 3161–3164.

(23) Giorgi, A. L.; Szklarz, E. G.; Storms, E. K.; Bowman, A. L.; Matthias, B. T. Effect of Composition on the Superconducting Transition Temperature of Tantalum Carbide and Niobium Carbide. *Phys. Rev.* **1962**, *125*, 837–838.

(24) Nakayama, H.; Ozaki, K.; Nabeta, T.; Nakajima, H. Composition Dependence of Lattice Parameter, Thermal and Electrical Properties in ZrC_x Compounds. *Mater. Trans.* **2017**, *58*, 852–856.

(25) Pauling, L. Atomic Radii and Interatomic Distances in Metals. *J. Am. Chem. Soc.* **1947**, *69*, 542–553.

(26) Fernández Guillermet, A.; Häglund, J.; Grimvall, G. Cohesive Properties of 4d-Transition-Metal Carbides and Nitrides in the NaCl-Type Structure. *Phys. Rev. B* **1992**, *45*, 11557–11567.

(27) Timoshenko, J.; Roldan Cuenya, B. *In Situ/Operando* Electrocatalyst Characterization by X-ray Absorption Spectroscopy. *Chem. Rev.* **2021**, *121*, 882–961.

(28) Zhang, H.; Jin, H.; Yang, Y.; Sun, F.; Liu, Y.; Du, X.; Zhang, Y.; Song, F.; Wang, J.; Wang, Y.; Jiang, Z. Understanding the Synergetic Interaction within α-MoC/β-Mo_2C Heterostructured Electrocatalyst. *J. Energy Chem.* **2019**, *35*, 66–70.

(29) Sun, X.; Yu, J.; Cao, S.; Zimina, A.; Sarma, B. B.; Grunwaldt, J. D.; Xu, H.; Li, S.; Liu, Y.; Sun, J. *In Situ* Investigations on Structural Evolutions during the Facile Synthesis of Cubic α-MoC_{1-x} Catalysts. *J. Am. Chem. Soc.* **2022**, *144*, 22589–22598.

(30) Ferralis, N. Probing Mechanical Properties of Graphene with Raman Spectroscopy. *J. Mat. Sci.* **2010**, *45*, 5135–5149.

(31) Finnemore, D. K.; Mapother, D. E.; Shaw, R. W. Critical Field Curve of Superconducting Mercury. *Phys. Rev.* **1960**, *118*, 127–131.

(32) Maki, K. Effect of Pauli Paramagnetism on Magnetic Properties of High-Field Superconductors. *Phys. Rev.* **1966**, *148*, 362–369.

(33) Brandt, E. H. Flux Distribution and Penetration Depth Measured by Muon Spin Rotation in High-Tc Superconductors. *Phys. Rev. B* **1988**, *37*, 2349–2352.

(34) Li, D.; Li, W. F.; Ma, S.; Zhang, Z. D. Electronic transport properties of NbC(C)-C nanocomposites. *Phys. Rev. B* **2006,** *73*, 193402.

(35) Tinkham, M. *Introduction to Superconductivity*. McGraw-Hill, Inc.: **1975**.

(36) Sarkar, S.; Kulkarni, N.; Kulkarni, R.; Thekkepat, K.; Waghmare, U.; Ayyub, P. Is There a Lower Size Limit for Superconductivity? *Nano Lett.* **2017**, *17*, 7027–7032.

(37) Wang, Z. H.; Li, D.; Geng, D.; Ma, S.; Liu, W.; Zhang, Z. D. Magnetic and Electronic Transport Properties of Nanocomposites of Superconducting Mo carbides' Nanoparticles Embedded in a Ferromagnetic Carbon Matrix. *J. Mater. Res.* **2009**, *24*, 2229–2234.

(38) Sánchez-Zacate, F. E.; Conde-Gallardo, A. Particle Size Effect on Lower Critical Field and Full Penetration Field in the $SmFeAsO_{0.91}F_{0.09}$ Superconductor. *Physica C* **2019**, *563*, 16–21.

(39) Bardeen, J.; Cooper, L. N.; Schrieffer, J. R. Theory of Superconductivity. *Phys. Rev.* **1957**, *108*, 1175–1204.

(40) Esch, B. von der; Peters, L. D. M.; Sauerland, L.; Ochsenfeld, C. Quantitative Comparison of Experimental and Computed IR-Spectra Extracted from Ab Initio Molecular Dynamics. *J. Chem. Theory Comput.* **2021,** *17*, 985–995.

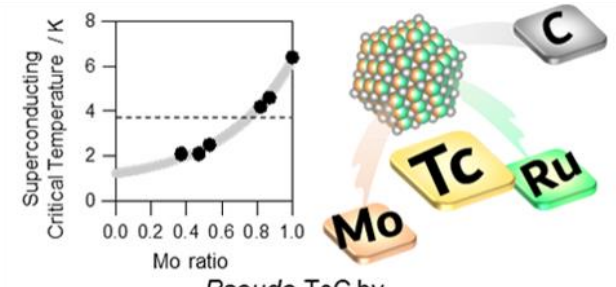

Pseudo-TcC by
Mo–Ru–C solid-solution alloy